The Astrophysical Journal, 899:133 (14pp), 2020 August 20 https://doi.org/10.3847/1538-4357/aba7b4

Nuclear Structures of ^{17}O and Time-dependent Sensitivity of the Weak *s*-process to the ^{16}O$(n,\gamma)^{17}$O Rate

Meng He[1,2], Shi-Sheng Zhang[1,2], Motohiko Kusakabe[1,2], Sizhe Xu[1], and Toshitaka Kajino[1,2,3]
[1] School of Physics, and International Research Center for Big-Bang Cosmology and Element Genesis, Beihang University, Beijing 100191, People's Republic of China; zss76@buaa.edu.cn, kusakabe@buaa.edu.cn, kajino@nao.ac.jp
[2] National Astronomical Observatory of Japan, 2-21-1 Osawa, Mitaka, Tokyo 181-8588, Japan
[3] Graduate School of Science, The University of Tokyo, 7-3-1 Hongo, Bunkyo-ku, Tokyo 113-0033, Japan
Received 2020 March 6; revised 2020 July 16; accepted 2020 July 19; published 2020 August 24

Abstract

We revisit the radiative neutron capture reaction ^{16}O$(n,\gamma)^{17}$O of astrophysical interest, based on the new reevaluated cross-section data. Several potentials are proposed to predict direct capture cross sections. The contributions from single-particle resonances to total capture cross section are quantitatively considered in Breit–Wigner formalism, taking into account the interference term between direct capture and resonant cross sections, which is crucial for the description of the behavior around the resonance energies. A new cross section is achieved based upon χ^2-fittings for optimized resonance parameters using Minuit code, and it has a largely improved agreement with updated experimental data. Statistical errors are also evaluated for the total and Maxwellian-averaged cross sections. It is confirmed that the direct captures dominate the total cross sections; however, resonant contribution also becomes progressively more important as the energy increases to 100 keV. Resonance contribution can increase the reaction rates for energy region 50 keV $< E <$ 100 keV by 5% ± 5%–25% ± 5%, and around 8% ± 5% in comparison with KADoNiS v0.3 rate and the latest data evaluations, respectively. We show a detailed propagation of the uncertainty in the ^{16}O(n,γ) reaction rate to abundances of nuclei, including *s*-nuclei during the weak *s*-process with a multi-zone nuclear network calculation. Although an enhanced rate of ^{16}O(n,γ) diminishes the *s*-process efficiency in the 25 $M_\odot$ stellar model adopted from the Modules for Experiments in Stellar Astrophysics, it can lead to larger abundances of neutrons as well as ^{22}Ne in the late epoch of C burning.

Unified Astronomy Thesaurus concepts: Helium burning (716); Carbon burning (7195); Reaction rates (2081); S-process (1419); Massive stars (732)

1. Introduction

About half of stable nuclei heavier than Fe originate from the slow neutron capture process (*s*-process) (Burbidge et al. 1957; Cameron 1957). The abundance distribution of *s*-nuclei in the solar system can be theoretically divided into three components: a "weak" ($60 < A < 90$) (Peters et al. 1972; Prantzos et al. 1990; Pignatari et al. 2010), a "main" ($90 < A < 208$) (Iben 1975; Truran & Iben 1977; Iben & Renzini 1982; Bisterzo et al. 2014; Karakas & Lugaro 2016), and a "strong" component (for half of the solar ^{208}Pb) (Gallino et al. 1998), which probably corresponds to the main *s*-process in a metal-poor environment. These are produced in different astrophysical sites with a wider and different range of temperatures, dynamical timescales, and neutron densities (e.g., Käppeler et al. 2011; Reifarth et al. 2014). The strength of the *s*-process reflects the neutron exposure or the neutron to seed ratio, which depend upon the *s*-process sites (e.g., Aoki et al. 2001).

The weak *s*-process occurs in massive stars with mass $M > 8M_\odot$ during the He core burning (Lamb et al. 1977) and later C shell burning (Raiteri et al. 1991, 1993; The et al. 2007). The neutrons fed during the weak *s*-process come mainly from the reaction ^{22}Ne$(\alpha, n)^{25}$Mg. The ^{22}Ne originates from ^{14}N accumulated in the H-burning epoch via ^{14}N(α,γ) ^{18}F$(,e^+ \nu_e)^{18}$O(α,γ). The dependence of the weak *s*-process in massive stars on the stellar metallicity has been investigated, and Prantzos et al. (1990) show that the weak *s*-process is not very sensitive to the metallicity, although there is a peak of *s*-process efficiency at the metallicity $Z/Z_\odot \sim 10^{-1}$–10^{-2}.

It was, however, pointed out that in fast-rotating metal-poor stars, the rotation affects stellar structure as well as mixing, so that the primary ^{14}N can be produced mostly via ^{12}C$(p,\gamma)^{13}$N$(,e^+ \nu_e)^{13}$C(p,γ) after the mixing of produced ^{12}C into the H-rich envelope (Meynet & Maeder 2002; Meynet et al. 2006; Hirschi 2007). Because this ^{14}N is converted to ^{22}Ne via ^{14}N$(\alpha,\gamma)^{18}$F$(,e^+ \nu_e)^{18}$O(α,γ) and the neutrons produced via ^{22}Ne(α, n) significantly boost the *s*-process, *s*-process nuclei are enriched in the rotating metal-poor stars (Pignatari et al. 2008; Frischknecht et al. 2010).

To derive accurate predictions of nucleosynthesis yields of *s*-nuclei, precise cross sections (CSs) are needed for neutron capture as well as charged particle reactions of light nuclei that operate in the He- and C-burning epochs (e.g., the ^{12}C+^{12}C fusion reaction; Bennett et al. 2010). Experimental measurements of neutron capture CSs have been performed at energies corresponding to stellar temperatures relevant for the *s*-process (e.g., Heil et al. 2008, 2009).

One of the neutron poisons during the weak *s*-process is ^{16}O (Mohr et al. 2016). If it absorbs a large amount of neutrons, the neutron flux is diminished so that the *s*-process becomes less efficient. Recently, sensitivity studies for the main *s*-process (Bisterzo et al. 2015; Koloczek et al. 2016) and weak *s*-process (Bennett et al. 2010; Nishimura et al. 2017) have been performed, which revive the significance of the reevaluation of the CS of the ^{16}O$(n,\gamma)^{17}$O reaction at astrophysical energies ($k_B T <$ 100 keV, k_B is Boltzmann constant) with direct captures (DCs) and resonance contributions being taken into account (Mohr et al. 2016). Their recommendations are lower, up to $k_B T = 60$ keV, compared with the previously recommended values, but up to 14% higher at $k_B T = 100$ keV. The impact of this different energy dependence on the weak

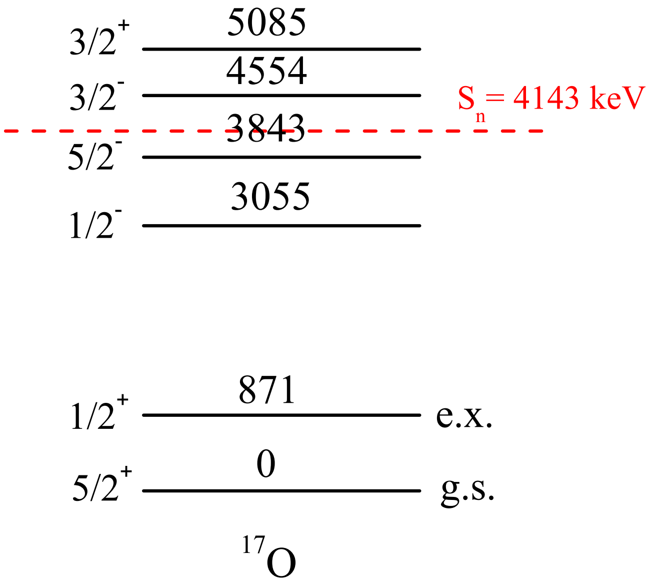

Figure 1. Bound and resonant structures for neutrons in ^{17}O with one-neutron separation energy $S_n = 4143$ keV (dashed red line).

s-process during He core burning ($k_B T = 26$ keV) and C shell burning ($k_B T = 90$ keV) in massive stars (25 $M_\odot$), where ^{16}O is the most abundant nuclide, is also discussed (Mohr et al. 2016).

Total CS consists of three mechanisms, e.g., DC, resonant capture (RC), and compound nucleus (CN) contributions. Statistical models are inappropriate when the number of available states in the compound system is relatively small. This is known to be the case for low-mass nuclei and those near-closed shells. Therefore, the contribution of two other mechanisms may become dominant through unbound levels with certain widths (RC) and direct electromagnetic transitions to bound levels (DC). It was shown through a simple analytical model (Mathews et al. 1983) that the DC contribution may dominate the total CS for nuclei with closed neutron shells or those with a low neutron binding energy. This model was reexamined (Zhang et al. 2015). A recent study (Xu & Goriely 2012) found that the E2 and M1 components are usually negligible with respect to the *E*1 contribution, although they dominate the DC rate for several hundred mid-shell nuclei. For simplicity, we mainly consider *E*1 contributions in our neutron capture CS calculations for nuclei near the closed shells.

As for the structures in ^{17}O as shown in Figure 1, previous Woods–Saxon (WS) potential (Huang et al. 2010) can reproduce level energy of ground state $1d_{5/2}$ and that of the first excited state $2s_{1/2}$. However, if one uses the same WS potential to calculate the resonant unbound orbital $1d_{3/2}$, it fails such that this orbital still remains bound, which contradicts with measured resonant state at $\sim$1 MeV. The resonances might play a crucial role in the reactions at high temperatures of astrophysical interest. For the last two decades, the CS data for ^{16}O(n,γ)^{17}O were not published after DC CS measurement (Igashira et al. 1995), and they were available only in private communications with different versions (Nagai et al. 1995; Mohr et al. 2016). Partly for this reason, although it was declared that they fit the data (Mohr et al. 2016), it is difficult to evaluate if the results are reliable enough, because the details of their fitting procedure are not written. However, the reanalysis of their measured data over the years (Igashira et al. 1995; Nagai et al. 1995) has been recently completed (Y. Nagai et al. 2020, in preparation). Therefore, we here adopt their new reevaluated CSs in our theoretical studies of the CS for ^{16}O(n,γ)^{17}O and apply them to the *s*-process nucleosynthesis in massive stars. We expect that even a small difference among different reaction rates might have some influence on nucleosynthesis. Here, we aim to reevaluate the capture CSs and reaction rates based on new data (Y. Nagai et al. 2020, in preparation) for radiative neutron capture reaction ^{16}O(n,γ)^{17}O.

We take into account the *E*1 transitions, i.e., from *p* wave scattering state to the ground state $1d_{5/2}$ and to the first excited state $2s_{1/2}$, resonant contributions, and the interference between the bound states and resonant states in the ^{16}O(n,γ)^{17}O reaction. We try to fully understand each contribution to the total CS, Maxwellian-averaged cross sections (MACS), and total reaction rates for a wider range of temperatures of astrophysical interest, so that we can analyze He and C burning in massive stars related to ^{16}O(n,γ)^{17}O reaction.

The paper is organized as follows. In Section 2, we first compare several potentials to find the best one for DC process. Subsequently, the contributions from single-particle (s.p.) resonances to total capture CS are quantitatively considered in Breit–Wigner formalism, together with the interference term between DC and resonant CSs being taken into account. We extract resonance parameters by fitting the updated data of total CS. Correspondingly, MACS is compared with the available data in other works. Their impacts on the nucleosynthesis is discussed in Section 3. Finally, we draw a brief summary in Section 4. In the Appendix, important production and destruction reactions of light nuclei during the C shell burning in a model star are shown.

2. Total CSs and Reaction Rates for ^{16}O(n,γ)^{17}O with DC and Resonance Contributions

2.1. Potentials for Direct Capture Cross Section (DCCS)

First, we need to find the best potential to reproduce DCCS for ^{16}O(n,γ)^{17}O reaction. We have adopted the Koning–Delaroche optical model potential (KD OMP) (Koning & Delaroche 2003) by using FRESCO code to calculate DCCS (Zhang et al. 2015), presented by dashed black line in Figure 2. It can be seen from this figure that the results from experimental bound states and scattering states in KD OMP, denoted by "Exp. + KD," underestimate DCCS compared with measured data, but agree with those results from microscopic Jeukenne–Lejeune–Mahaux OMP (Jeukenne et al. 1977). We also use RADCAP and FRESCO codes to calculate DCCS with the real part of KD OMP. Because this real potential cannot reproduce the s.p. levels for the ground state $1d_{5/2}$ and the first excited state $2s_{1/2}$, we adjust depth of the potential ($V_0 = -58.65$ MeV) in the volume part and that of the spin–orbit potential ($V_{ls} = -11.95$ MeV) to reproduce the s.p. level energies with positive parity, such as the ground state $1d_{5/2}$ with -4.17 MeV, the first excited state $2s_{1/2}$ with -3.54 MeV, and the resonant orbital $1d_{3/2}$ with 946 keV. We note that imaginary part and surface potential in KD OMP are ignored in a new fitting WS potential. We point out that the RADCAP code still cannot give reasonable results for s.p. resonant orbital $2p_{3/2}$ in such a new WS potential, which is probably because our potential model does not include the particle-hole excitation in the ^{16}O core, so that the low-lying negative parity states (e.g., $2p_{3/2}$) are not reproduced (Yamamoto et al. 2009). Interestingly, however, we found that the predictions of

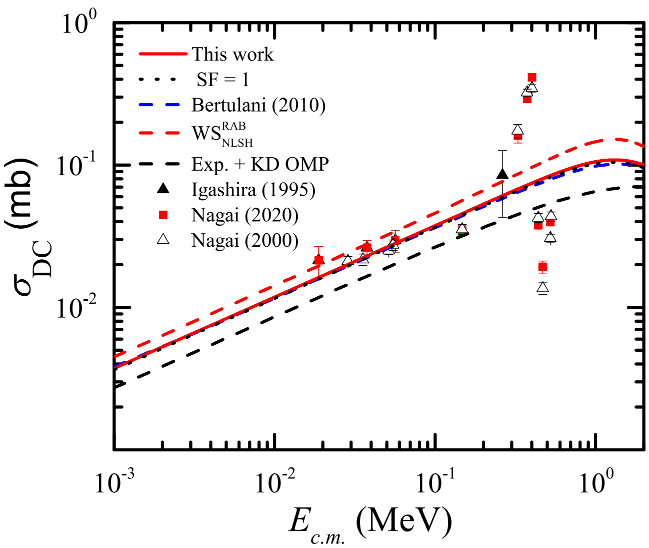

Figure 2. DCCS of $^{16}O(n,\gamma)^{17}O$ calculated by using RADCAP code with adjusted WS potential (solid red line; dotted black line with SF = 1) based on KD OMP, with WS potential (dashed blue line, Huang et al. 2010), those with WS potential fitted with the last neutron level given by RAB method for NLSH interaction (dashed red line, S.-S. Zhang et al. 2020, in preparation), and those using FRESCO code with KD OMP (dashed black line, Zhang et al. 2015). Experimental data for low-energy capture cross sections (black triangles, Igashira et al. 1995; black hollow triangles, Y. Nagai 2000, private communication) and those for total cross sections with single-particle resonance $2p_{3/2}$ scattered around 411 keV resonance (red squares, Y. Nagai et al. 2020, in preparation).

DCCS (dotted black line) in this potential, denoted by "SF = 1" in Figure 2, agree with the experimental data (Igashira et al. 1995) at low energies. Corresponding results with spectroscopic factor (SF) extracted from the fitting procedure described in the next subsection are shown by "This work" with a solid red line. The predictions with WS potential (dashed blue line, Huang et al. 2010) are amazingly close to those from adjusted WS potential. It needs to be noted that the potential of Huang et al. (2010) cannot describe the resonances, but our new WS potential can reproduce $1d_{3/2}$.

The evaluations using the available RADCAP code with the WS potential that fits the valence neutron level the microscopic covariant density functional RAB method of S.-S. Zhang et al. (2020, in preparation) with the nonlinear effective interaction proposed by Sharma et al. (1993; NLSH) are also presented by a dashed red line for comparison. It seems to overestimate the DCCS, but can reproduce $1d_{3/2}$ $E_R\sim$ with around 1 MeV close to the measured 0.942 MeV, which is also confirmed by Green's function method within the same framework (Sun et al. 2014). We also try Xu's OMP (Xu et al. 2016), which gives $E_R\sim$ around 0.3 MeV above the threshold, but the real part of this potential cannot describe the bound states. Therefore, two WS potentials among five potentials are proper to describe DCCS, which dominates MACS in the temperature region $k_B T <$ 100 keV. Because there is no available uniformed potential to describe both bound and resonant states simultaneously for the moment, we simply use the measured energies and widths for s.p. resonant states $2p_{3/2}$ and $1d_{3/2}$ for the later calculations.

2.2. Total CSs with Non-resonant DC, Resonance, and Interference Terms

For the resonant CSs, several measurements provide the resonant energies and widths for s.p. resonant states (Mohr et al. 2016). Mohr et al. (2016) have derived parameters $E_R = 411$ keV and $\Gamma_n = 42.5 \pm 5$ keV for $2p_{3/2}$ orbital, and $E_R = 942$ keV and $\Gamma_n = 96 \pm 5$ keV for the $1d_{3/2}$ orbital, based on the measurements. However, the ambiguity of the determination for resonance shape still exists if one notices the data around 300 keV. Moreover, details of fitting procedures are unknown because they did not show the fitting parameters. The evolution of a massive star needs precise knowledge of the reaction rates, which depend strongly on the resonant contributions. Therefore, we reevaluate the total CSs very carefully by taking account of theoretical non-resonant DC CSs, resonant CSs, and the interference term between the DC background and resonant scattering in the following expressions,

$$\sigma_T(E) = \sigma_{DC}(E) + \sigma_R(E) + 2\sqrt{\sigma_{DC}(E)\sigma_R(E)}\cos\delta_R(E), \quad (1)$$

in which the resonant CS $\sigma_R(E)$ takes the form of Breit–Wigner formalism,

$$\sigma_R(E) = \frac{\pi\hbar^2}{2\mu E}\frac{2J_R+1}{(2J_a+1)(2J_b+1)}\frac{\Gamma_l(E)\Gamma_\gamma}{(E-E_R)^2+(\Gamma_{tot}/2)^2}, \quad (2)$$

and the phase shift fulfills

$$\delta_R(E) = \arctan\frac{\Gamma_l(E)}{2(E_R-E)}, \quad (3)$$

where $\hbar$ is the reduced Planck constant, E_R is the resonance energy, and J_R, J_a, J_b are the spins of the resonance and the projectile $a = n$ and target $b = {}^{16}O$, respectively. The total width Γ_{tot} is the sum of the particle decay partial width Γ_l with orbital angular momentum $l\hbar$ and the γ-ray partial width Γ_γ; $\Gamma_{tot} = \Gamma_l(E)+\Gamma_\gamma$. A decay width of a nuclear state can be written as (Clayton 1984)

$$\Gamma_l(E) = 3\frac{\hbar c}{R}\sqrt{\frac{2E}{\mu c^2}}P_l\Theta_l^2, \quad (4)$$

where c is the light speed, Θ_l^2 is the reduced width, R is the channel radius set equal to $R = 2.6$ fm (Ozawa et al. 2001), μ is the reduced mass of the incident channel, and P_l is penetration factor (Trkov & Brown 2018), which takes the form of $P_l = \rho^3/(1+\rho^2)$ for $l = 1$ and $P_l = \rho^5/(9+3\rho^2+\rho^4)$ for $l = 2$, $\rho = \kappa R$ with the wavenumber κ.

Actually, as mentioned in the previous subsection, because there is not any available potential to describe the p wave resonant state $2p_{3/2}$ appropriately, we have adopted the channel radius R so that the resonance energy E_R and width $\Gamma_l(E_R)$ can reproduce the measured values with a fixed reduced width Θ_l^2. In this way, $\Gamma_l(E)$ can be expressed as the function of energy E, which plays an important role in resonant CSs. If we simply suppose $\Gamma_l(E)$ as a constant, then the resonant CSs in a lower-energy region, for example $E < 100$ keV, is artificially enhanced. This is obviously not reasonable from a physical point of view. Therefore, we use $\Gamma_l(E)$ in Breit–Wigner formalism and the expression of the phase shift in the interference term as well. The interference term in Equation (1) is also crucial for the CS behavior nearby the resonance energy. One cannot reproduce the experimental data below and above the resonance energies without the interference between DC and resonance, as is discussed below.

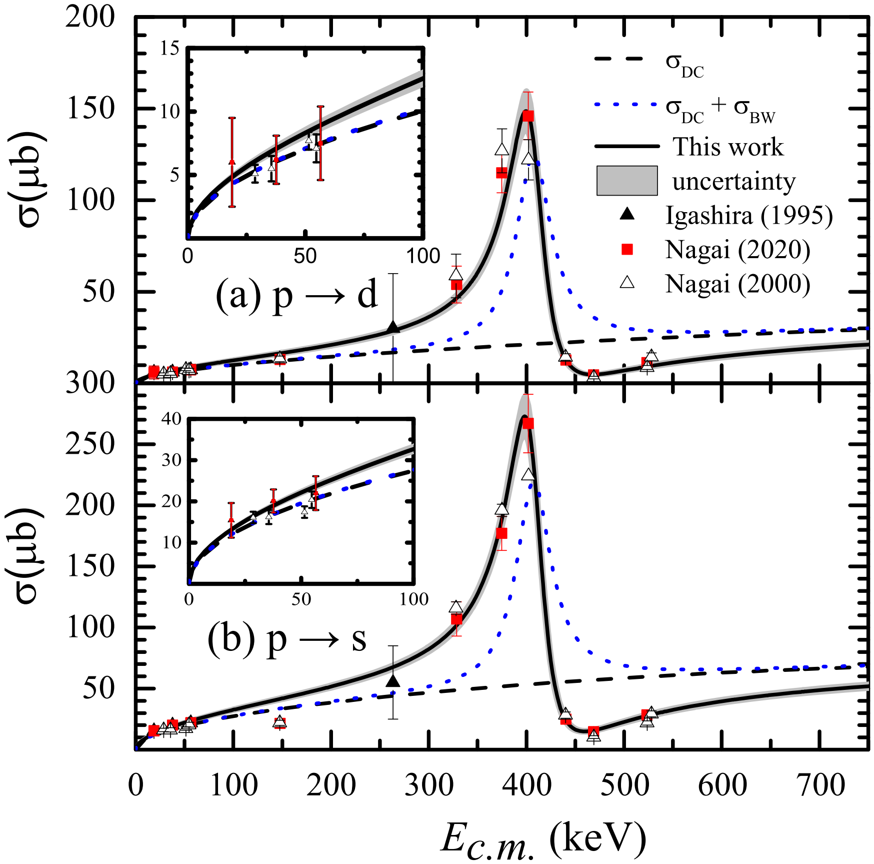

Figure 3. (a) Experimental data for the ground-state transition of the $^{16}O(n,\gamma)^{17}O$ reaction (black triangles, Igashira et al. 1995; red squares, Y. Nagai et al. 2020, in preparation; and black hollow triangles, Y. Nagai 2000, private communication). Fitting results (solid black line) with spectroscopic factors listed in Table 1 and the ultimate uncertainty (gray band) are displayed. Dashed black line refers to the DCCS σ_{DC}, and dotted blue line refers to the summation of DC and resonant cross sections $\sigma_{DC} + \sigma_R$. (b) Same as panel (a), but for the transition to the first excited state ($1/2^+$, $E^* = 871$ keV). The inset enlarges the most relevant energy region below 100 keV for astrophysical application. References and symbols are the same as Figure 2.

Table 1
Optimum Parameters: Resonance Energy E_r, Reduced Width Θ_l^2, Gamma Partial Widths $\Gamma_{\gamma,0}$ and $\Gamma_{\gamma,1}$, Spectroscopic Factors C^2S_0 and C^2S_1

E_r(keV)	Θ_l^2	Γ_n(keV)	$\Gamma_{\gamma,0}$(eV)	$\Gamma_{\gamma,1}$(eV)	C^2S_0	C^2S_1	L
409.0 ± 1.65	0.161 ± 0.009	44.1 ± 2.6	0.33 ± 0.03	0.54 ± 0.04	1.159 ± 0.065	0.984 ± 0.037	0.760

We use Minuit code (http://www.cern.ch/minuit), a physics analysis tool for function minimization, to fit the updated data by minimizing the objective function with multiple parameters. We define objective function as

$$L = \frac{1}{n}\sum_{i=1}^{n}\frac{[\sigma_T(E_i;\, E_r,\, \Theta_l^2,\, \Gamma_{\gamma,0},\, C^2S_0,\, \Gamma_{\gamma,1},\, C^2S_1) - \sigma_{\mathrm{Exp},i}]^2}{\Delta_i^2}, \tag{5}$$

where $\sigma_{\mathrm{Exp},i}$ refers to experimental data of total CS at the neutron incident energy E_i, with the value of error bar Δ_i, $\sigma_T(E_i;\, E_r,\, \Theta_l^2,\, \Gamma_{\gamma,0},\, C^2S_0,\, \Gamma_{\gamma,1},\, C^2S_1)$ is the theoretical prediction of the total CS, and n corresponds to the number of experimental data. There are six parameters in total, E_r, Θ_l^2, $\Gamma_{\gamma,0}$, $\Gamma_{\gamma,1}$, C^2S_0, and C^2S_1 (resonance energy, reduced width, gamma partial widths, and SFs from scattering p wave, where the subscript 0 and 1 specifies the final state, i.e., the ground state $1d_{5/2}$ and the first excited state $2s_{1/2}$, respectively). During the fitting procedure, they are adjusted to minimize the objective function L. In the search for the best parameter set, the iteration of the estimate for the function stops when the relative decrement $|L(m+1) - L(m)|/L(m)$ reaches 10^{-6}. The uncertainty of the CS is obtained as the square root of the sum of partial squares of uncertainties from respective parameters.

We list optimum parameters in Table 1 derived by fitting the updated experimental data (Y. Nagai et al. 2020, in preparation). In this fit, an outlier datum at $E = 148$ keV for the transition to the first excited state has been excluded, which shows a large deviation from our fitted result (Figure 3(b)) as well as that of Mohr et al. (2016). That datum accounts for a very large part of the function L, and when it is excluded from the fit the L value decreases by $\Delta L = -2.98$. Furthermore, it is confirmed that the derived parameter set fits the data better than that of Mohr et al. (2016) by $\Delta L = -1.26$, or $\Delta\chi^2 = 19\Delta L = -23.9$ when the outlier is excluded. Our best fit of $\Gamma_{\gamma,0} = 0.33$ eV is close to 0.42 eV (Holt et al. 1978, Table A1) or 0.4 eV from a $^{17}O(\gamma, n)^{16}O$ experiment (Holt et al. 1978). For different neutron incident energy, the uncertainty of total CS is different. Around the resonance peak (410–450 keV), it is larger than 10%, and at most 17%. In the lower-energy region, the uncertainty diminishes as low as ∼4%.

From the scattering p wave, neutron is captured with electric dipole radiation ($E1$) into the ground state $1d_{5/2}$ and into the first excited state $2s_{1/2}$, which are respectively displayed in Figures 3(a) and (b). It can be seen that the DCCS to the first excited state $2s_{1/2}$ is larger than that to the ground state $1d_{5/2}$. This is because the radial wave function of the $2s_{1/2}$ excited state with one radial node extends to the surface region farther than the $1d_{5/2}$ ground-state wave function without radial node does, so that the overlap of the wave functions between the incident p wave at low energies of astrophysical interest becomes much larger for the $2s_{1/2}$ state than that for the $1d_{5/2}$ state. As a result, the matrix elements overcome the difference due to the Q-values as well as the spin factors ($2J_f$+1), which are 2 and 6 for the final state $f = 2s_{1/2}$ and $1d_{5/2}$, respectively.

The solid black lines in Figure 3 refer to our fitting results of the total CSs based on the updated experimental data (Y. Nagai et al. 2020, in preparation). The gray band refers to the range of the uncertainty. It can be clearly seen that the large errors occur around the resonance peak. From the numerical results, the upper and lower limits of the uncertainty appear above the resonance energy for orbital $2p_{3/2}$, about ±16%. The resonant contribution to the low-energy region below 100 keV is small enough that it does not significantly influence the total CS due to the very small penetration factor in $\Gamma_l(E)$ for p wave neutron in Equation (4). If one uses a constant width Γ_l (42.5 keV for $2p_{3/2}$ and 96 keV for $1d_{3/2}$), the resonant CS below the resonance energy will be artificially enhanced greatly, which is not reasonable from physical picture of the resonance. Moreover, the interference term in Equation (1) plays so crucial a role that the total CSs at the energies larger than the resonance are reproduced very well only when this interference term is taken into account, as is clearly demonstrated by the solid black lines in Figure 3. Simple coherent sum $\sigma_{\rm DC}$+$\sigma_{\rm R}$ (dotted blue lines) of the DCCS $\sigma_{\rm DC}$ (dashed black lines) and the resonant CSs $\sigma_{\rm R}$ extremely overproduces the total CSs in this energy region.

To clarify the predictions for the low-energy part, we magnify the plots below 100 keV and display them in the inset plots of Figure 3, where it can be seen that the interference term increases the theoretical predictions at this low-energy region, but still in the error bar of the experimental data. One can see the slight shift of the peak caused by the interference term, near the resonance energy (see the solid black and dotted blue lines in Figure 3). We should emphasize that $\Gamma_l(E)$ and the interference term make the predictions agree with the update data, and even better than the fitting results of Mohr et al. (2016). Then we want to see the effects on nucleosynthesis in massive stars that might arise from the difference between Mohr's and our theoretical radiative capture CSs for ^{16}O(n,γ)^{17}O quantitatively. The key point for the calculations in agreement with the measured data owes to $\Gamma_l(E)$, which appears in Breit–Wigner formalism and the phase shift in the interference term. In this way, the behavior below and above the resonances are naturally described and the contributions to the lower-energy part $E < 100$ keV are properly and effectively depressed or controlled. Furthermore, our predictions are larger than Mohr's calculations (Mohr et al. 2016) below the resonance energy of astrophysical interest.

Figure 4 displays the total CS σ_T of ^{16}O (n, γ)^{17}O for wider energy region from 10^{-3} keV to 10^3 keV, based on the best fit

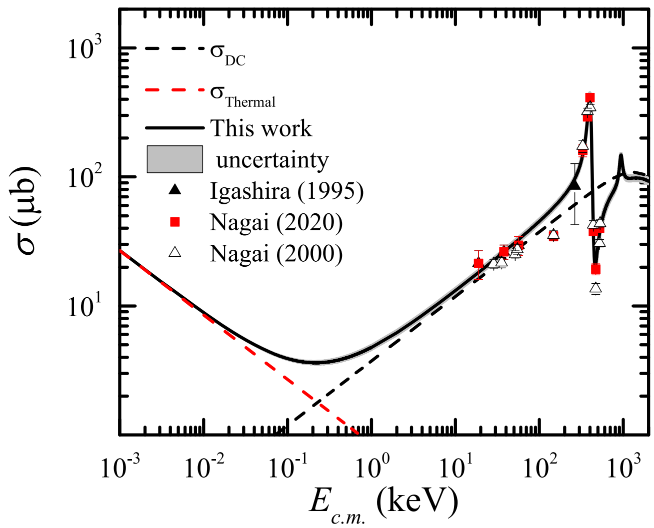

Figure 4. Total cross section of ^{16}O(n,γ)^{17}O, including the s wave component constrained from the thermal neutron cross sections σ_0, DCCS (transition from scattering p wave to ground state d wave and that of the first excited state s wave) and resonance cross sections for s.p. resonant orbitals $2p_{3/2}$ and $1d_{3/2}$. References and symbols are the same as Figure 2.

of updated data. Because the thermal neutron capture CS was updated (Firestone & Revay 2016), we use the latest value $\sigma_0 = 0.170 \pm 0.003$ mb in σ_T corresponding to the electric dipole ($E1$) transition (Firestone & Revay 2016). In Figure 4, the total CS σ_T includes the s wave component determined from thermal neutron CSs σ_0 (dashed red line), non-resonant DCCS $\sigma_{\rm DC}$ (dashed black line) from scattering p wave to the ground state d wave and the first excited state s wave, and resonance CSs for s.p. resonant orbitals $2p_{3/2}$ and $1d_{3/2}$. As for the resonant contributions, the solid black line refers to σ_T with $\Gamma_l(E)$. The resonance energy for $1d_{3/2}$ orbital equals to 942 keV with neutron resonance width $\Gamma_n = 96$ keV, and γ width $\Gamma_\gamma = 1$ eV. The procedure to calculate resonant CSs for $1d_{3/2}$ is the same as that for $2p_{3/2}$, as described above.

2.3. MACSs and Thermal Reaction Rates

Before we calculate reaction rates for the network simulations, we study the MACS by the expression

$$<\sigma>_{k_{\rm B}T} = \frac{2}{\sqrt{\pi}}\frac{1}{(k_B T)^2}\int_0^\infty \sigma(E) E \exp\left(-\frac{E}{k_B T}\right) dE. \quad (6)$$

In Figure 5, we show the MACS of ^{16}O (n, γ)^{17}O calculated by Equation (6) on the upper panel (a), and the ratios to KADoNiS v0.3 rate (blue lines) and Mohr's predictions (red lines) on the lower panel (b). In Figure 5(a), the dashed black line denotes the DC MACS. The solid black line refers to the MACS in this work. The blue and red solid lines refer to those from KADoNiS v0.3 rate and Mohr's results, respectively. All these lines are larger than the DC MACS, which includes the only transition from scattering p wave to the bound states, i.e., the ground state $1d_{5/2}$ and the first excited state $2s_{1/2}$ without resonant contribution through the $3/2^-$ state at 411 keV. Our predictions (solid black line) are obviously larger than those from KADoNiS v0.3 rate (solid blue line) and Mohr's results (solid red line). The fact is particularly natural because Mohr's fit underestimates the measured CSs for the energy region below the $3/2^-$ resonance ($E_R = 411$ keV), whereas our evaluations smoothly describe the data (see Figure 3).

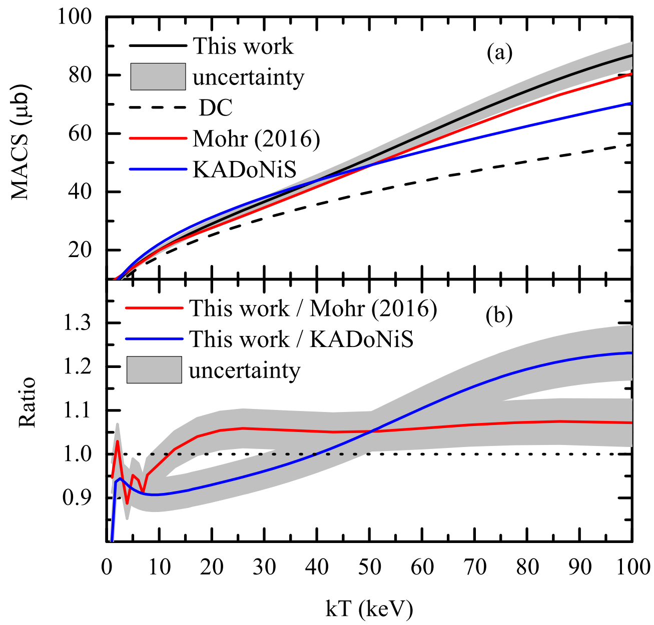

Figure 5. (a) Maxwellian-averaged cross sections of $^{16}O(n,\gamma)^{17}O$ and (b) the ratio of the derived rate to KADoNiS v0.3 rate and results of Mohr et al. (2016). On panel (a): the dashed black line denotes the DC MACS; the solid black line refers to the total MACS in this work with the uncertainty (gray band); the solid blue (red) line refers to that from KADoNiS v0.3 rate (Mohr's results). On panel (b): the ratios of our predictions to those from KADoNiS v0.3 rate (solid blue lines) and Mohr's results (solid red lines). Dotted black line corresponds to ratio 1.0.

For detailed and quantitative comparison, we show the ratios of our predictions relative to the MACS from KADoNiS v0.3 rate and Mohr's results in Figure 5(b). Our result is larger than KADoNiS v0.3 rate and Mohr's results in the energy regions $10\,\mathrm{keV} < k_B T < 100\,\mathrm{keV}$ and $40\,\mathrm{keV} < k_B T < 100\,\mathrm{keV}$, respectively. Specifically, our result is larger than those in KADoNiS v0.3 rate and Mohr's predictions by 10%–25% and ∼10%, respectively, for the energy region $k_B T > 70$ keV.

The thermal reaction rates related to MACS are given here for the application to the network calculation of nucleosynthesis in the next section,

$$N_A < \sigma v > = N_A < \sigma >_{k_B T} \quad v_{k_B T}, \tag{7}$$

where $\langle \sigma v \rangle$ means to take the Maxwellian average of the reaction rate $\sigma\,(E)\,v$, N_A is the Avogadro number, $\langle \sigma \rangle_{k_B T}$ is the MACS defined by Equation (6), and $v_{k_B T}$ is the thermal velocity $v_{k_B T} = \sqrt{2k_B T/\mu}$. Because the MACS is equivalent to the thermal reaction rate except for the prefactor, i.e., $\langle \sigma v \rangle = \langle \sigma \rangle_{k_B T} v_{k_B T}$, all discussions of the MACS for several different estimates of the CSs for $^{16}O\ (n,\gamma)^{17}O$ apply to the thermal reaction rates with respect to the temperature. The corresponding temperature is connected from the thermal energy according to $E = T_9/11.605$, where T_9 is the temperature in units of GK, i.e., $T_9 = T/(10^9\ \mathrm{K})$, and E is in units of MeV. The final recommended rate of the present study remains within the uncertainty band of Mohr's recommendation (−10%, +20%).

3. Effect on the Weak *s*-process

3.1. Nuclear Reaction Network

We investigate the sensitivity of weak *s*-process to the reaction rate for $^{16}O(n,\gamma)^{17}O$ by post-process nucleosynthesis calculations using a result from the Modules for Experiments in Stellar Astrophysics (MESA, version r11701) (Paxton et al. 2011, 2015, 2018, 2019), with MESA SDK for Linux (Version 20190503) by Richard Townsend (2019). The MESA equation of state (EOS) is a blend of the OPAL (Rogers & Nayfonov 2002), SCVH (Saumon et al. 1995), PTEH (Pols et al. 1995), HELM (Timmes & Swesty 2000), and PC (Potekhin & Chabrier 2010) EOSs. Radiative opacities are primarily from OPAL (Iglesias & Rogers 1993, 1996), with low-temperature data from Ferguson et al. (2005) and the high temperature, Compton-scattering dominated regime by Buchler & Yueh (1976). Electron conduction opacities are from Cassisi et al. (2007). MESA includes nuclear reaction rates from JINA REACLIB (Cyburt et al. 2010) plus additional weak reaction rates (Fuller et al. 1985; Oda et al. 1994; Langanke & Martinez-Pinedo 2000), screening (Chugunov et al. 2007), and thermal neutrino loss rates (Itoh et al. 1996).

We perform simple multi-zone nucleosynthesis calculations with the MESA result for a test suite: 25M_pre_ms_to_core_collapse.[4] The evolution of nuclear abundances are calculated at respective zones of MESA, and an instantaneous mixing is assumed within mixing zones. The network includes 1963 nuclides composed of enough large numbers of isotopes for respective elements from $_1H$ to $_{84}Po$. Nuclear data for the reaction network calculations are taken from JINA REACLIB (Version 2.0 taken in 2014) (Cyburt et al. 2010). Rates for the radiative neutron capture, i.e., (n,γ), are taken from KADoNiS v0.3 (3rd update of Karlsruhe Astrophys. Database of Nucleosynthesis in Stars) (Bao et al. 2000; Dillmann et al. 2006a, 2009), except for $^{16}O\ (n,\gamma)^{17}$ O. Rates for the β^- decay, and the β^+ decay plus the electron capture, are taken from Takahashi & Yokoi (1987), and supplemented by JINA REACLIB data. The α-decay rates are taken from the Nuclear Wallet Cards (2011).[5] We note that nuclear decays with branching ratios of $<10^{-3}$ are neglected in this study. Rates of other reactions, i.e., those between charged light nuclei up to $_{28}Ni$, are taken from the JINA REACLIB. The solar abundance is adopted from Lodders et al. (2009).

3.2. Results

The stellar nucleosynthesis is calculated for two cases of $^{16}O(n,\gamma)^{17}O$ as discussed in Section 2: (1) the "standard" rate with an uncertainty estimated, and (2) the KADoNiS rate (Dillmann et al. 2009) (fitted by JINA REACLIB). The rates for the inverse reaction $^{17}O(\gamma,n)^{16}O$ are input so that the principle of detailed balance between the forward and reverse reaction rates is satisfied in the two cases, respectively.

Table 2 shows coefficients of the REACLIB analytical function for the forward reaction rates of $^{16}O(n,\gamma)^{17}O$, i.e., a_i ($i = 0$–6), in the two cases. The function is given by

$$N_A \langle \sigma v \rangle = \exp\left[a_0 + \frac{a_1}{T_9} + \frac{a_2}{T_9^{1/3}} + a_3 T_9^{1/3} + a_4 T_9 + a_5 T_9^{5/3} + a_6 \ln T_9\right] (\mathrm{cm^3\ mol^{-1}\ s^{-1}}). \tag{8}$$

[4] We directly adopted this result. Physical parameters are unchanged from the default setting. However, the frequency of output has been increased in list, and MESA was reinstalled accordingly. In addition, the initial ^3He abundance is different from the solar abundance, and outputs for ^{20}Ne abundance look to include ^{22}Ne abundance. Therefore, we do not use the abundances of ^3He and ^{20}Ne from MESA in our post-process calculations.

[5] https://www.nndc.bnl.gov/nudat2/indx_sigma.jsp

Table 2
Fitted Reaction Rates Applicable for $T_9 \leqslant 5$

Coefficient	a_0	a_1	a_2	a_3	a_4	a_5	a_6
Standard	−9.209829e+00	3.398355e−02	−5.704789e+00	2.849638e+01	−4.202927e+00	4.657980e−01	−6.791892e+00
upper limit	−9.994766e+00	3.628833e−02	−6.047378e+00	2.979724e+01	−4.345263e+00	4.786021e−01	−7.204740e+00
lower limit	−8.368539e+00	3.154310e−02	−5.340908e+00	2.710610e+01	−4.049982e+00	4.519828e−01	−6.352013e+00
KADoNiS (JINA REACLIB)	7.215460e+00	2.350150e−02	−2.112460e+00	4.877420e+00	−3.144260e−01	1.695150e−02	−9.847840e−01
$E_r = 1.24$ MeV	1.237180e+01	−1.433854e+01	0.0	0.0	0.0	0.0	−1.500000e+00
$E_r = 1.55$ MeV	1.351694e+01	−1.802947e+01	0.0	0.0	0.0	0.0	−1.500000e+00

For the reverse reaction rates, the function is given by

$$n_\gamma(T)\langle\sigma_{(\gamma,n)}c\rangle = \exp\left[b_0 + \frac{b_1}{T_9} + \frac{b_2}{T_9^{1/3}} + b_3 T_9^{1/3} + b_4 T_9 + b_5 T_9^{5/3} + b_6 \ln T_9\right] (\mathrm{s}^{-1}), \quad (9)$$

where $n_\gamma(T)$ is the photon number density, $\sigma_{(\gamma,\ n)}$ is the photodisintegration CS for ^{17}O(γ, n)^{16}O, and the coefficients b_i ($i = 0$ to 6) are related to a_i via $b_0 = a_0 + 21.823060$, $b_1 = a_1 - 48.081817$, $b_j = a_j$ (for $j = 2$ to 5), and $b_6 = a_6 + 1.5$. Reaction rates corresponding to the upper and lower limits are also shown. Resonant components for $E_X = 5.38$ and 5.79 MeV are separately listed, which are derived from widths for γ-decay into the ground state measured by Johnson et al. (1979). These additional components do not affect the total rate at low temperatures in the weak s-process. However, the sum of the standard rate with the additional resonant components is applicable up to $T_9 = 5$, and therefore useful in general nucleosynthesis calculations.

Figure 6 (panels (a)–(c)) shows time evolutions of physical quantities of a star with initial mass 25 $M_\odot$ and solar metallicity during the core He burning at the stellar center with the standard rate of ^{16}O(n,γ)^{17}O. Panels (a) and (b) correspond to temperature and density, and nuclear mass fractions, respectively. At the stellar age of $t \sim 6.4$ Myr, the H burning completes and the ^{4}He burning starts (panel (b)). Then, the central temperature and density increase (panel (a)). Because the He core is fully convective, it is always mixed with the outer region. Along with the evolution of mixing zone boundary, zigzag patterns are seen in abundances of less abundant species. The ^{14}N nuclei originating from initial CNO are efficiently converted to ^{22}Ne via radiative α captures, and ^{13}C is burned via (α, n) at $t \sim 6.4$ Myr. The weak s-process is predominantly triggered by neutrons generated via the ^{22}Ne(α, n) reaction in the late epoch of He burning. This is seen in a decrease of the abundance of the dominant seed ^{56}Fe, and increases of abundances of products of the s-process, i.e., ^{57}Fe and ^{70}Ge.

Figure 6(c) shows the neutron mole fraction Y_n as a function of time. There is a sharp peak caused by ^{13}C(α, n) at $t \sim 6.4$ Myr, and a later gradual increase via the reaction ^{22}Ne(α, n). The temperature increases from $T_9 \sim 0.05$ to 0.2 at $t \sim 6.4$ Myr. In this range, the difference in the rates between the "standard" and "KADoNiS" rates is $\sim-(8\text{–}10)\%$. Because of the increasing MACS or equivalently thermonuclear reaction rate of ^{16}O(n,γ)^{17}O as a function of T (see Figure 5), this neutron capture gradually becomes important. It becomes the largest neutron capture reaction rate from $t \sim 6.9$ Myr. At the end of increasing Y_n at $t \lesssim 7.1$ Myr, the rate of the reaction ^{16}O(n,γ)^{17}O accounts for about 40% of the total destruction rate of neutrons. However, the difference in the Y_n values during the core He burning is rather small because of the small difference in the reaction rate at low temperatures.

Figure 7 shows time evolutions of the same physical quantities of the model star as in Figure 6, but during the shell C burning at a fixed Lagrangian mass $M_r = 2M_\odot$. The time is measured in the inverse direction as $t_{\rm Si} - t$, where $t_{\rm Si}$ is the time for the onset of core Si burning. Toward $t_{\rm Si}$, the stellar evolution rapidly proceeds, and at $t_{\rm Si} - t \lesssim 1$ yr, the ^{12}C abundance decreases via the C burning (Figure 7(b)). The ^{22}Ne abundance also decreases via ^{22}Ne(α, n)^{25}Mg induced by α-particles from ^{12}C(^{12}C,α)^{20}Ne. This triggers the second round of the s-process, which converts seed nuclei ^{56,57}Fe into s-nuclei like ^{70}Ge (Figure 7(b)) when the neutron abundance stays at high value (Figure 7(c)).

Figure 8 shows deviations from unity of ratios of mole fractions of neutron, ^{4}He, ^{17,18}O, ^{20,21,22}Ne, and ^{25}Mg in the standard and KADoNiS cases. Effects of the uncertainty in the ^{16}O(n,γ) rate are interpreted from time evolution of abundance change rates, i.e., $|dY_i/dt|$ in the Appendix.

After the onset of the second round of the s-process, the temperature is as high as $T_9 \gtrsim 1$ and ^{16}O is again the strongest neutron poison, and accounts for about one-third of the total neutron destruction rate. There are subdominant contributions from ^{25}Mg(n,γ), ^{20}Ne(n,γ), ^{24}Mg(n,γ), ^{23}Na(n,γ), and so on, due to relatively high abundances of target nuclei. At $T_9 \gtrsim 1$, the "standard" rate of ^{16}O(n,γ)^{17}O is higher than the KADoNiS rate by $\sim$20%.

Response of the Y_n value to the change of the reaction rate for ^{16}O(n,γ)^{17}O is interesting. From Figure 7(b), we can read off the fact that the effective C burning starts at around $t_{\rm Si} - t \approx 0.5$ yr when the ^{12}C abundance decreases drastically. If we increase the reaction rates for ^{16}O(n,γ)^{17}O, the Y_n value is at first lower, but becomes higher at $t_{\rm Si} - t \lesssim 0.2$ yr (Figure 8). This increase in Y_n for larger reaction rates seems counterintuitive because more rapid consumption of neutrons is naively expected by larger rates. However, this happens because of time evolution of light nuclear abundances via the network (see the Appendix). As the temperature and density increase toward $t_{\rm Si} - t \approx 0.5$ yr, the s-process proceeds significantly and the seed composition evolves as shown in Figure 7(b). At the C shell burning, ^{22}Ne is predominantly destroyed via ^{22}Ne(α, n)^{25}Mg. When the ^{16}O(n,γ)^{17}O rate is larger, the ^{17}O abundance is larger and the reaction ^{17}O(α, n)^{20}Ne (Best et al. 2013) consumes more α particles generated by the C+C fusion. As a result, more ^{22}Ne nuclei survive destruction via ^{22}Ne(α, n)^{25}Mg. The Y_n value is then more associated with the larger neutron supply via the ^{22}Ne(α, n)^{25}Mg reaction in the late epoch.

Figure 9(a) shows overproduction factors of stable nuclei as a function of mass number A, at the stellar center after the core He burning in the standard rate case. Red filled circles and blue triangles indicate s-only nuclei and p-nuclei, respectively, while black open circles indicate other stable nuclei. During the weak s-process of the core He burning, abundances of some nuclei are enhanced. Especially, a global trend of overproduction is seen for $A \lesssim 90$. For heavier mass, i.e., $A \gtrsim 90$, overproduction factors scatter around the line of $X/X_\odot = 1$. However, all of s-only nuclei are overproduced. The p-nuclei show a large variation. Some of them are just destroyed via the neutron capture, and the others are produced via a combination of the neutron capture and β-decay.

Figure 9(b) shows ratios of overproduction factors in the standard and KADoNiS cases as a function of A. Red filled circles (s-only nuclei) and open circles (other stable nuclei) are plotted. Ranges of results for the upper and lower bound cases are shown with vertical bars. The s-only nuclei are located on the general trend of stable nuclei. Although deviations from unity are seen, they are smaller than the change in the reaction rate of ^{16}O(n,γ)^{17}O because the rate is relatively small in the temperature range of $0.05 \lesssim T_9 \lesssim 0.2$ for the He-burning s-process and the resultant change of neutron abundance is small.

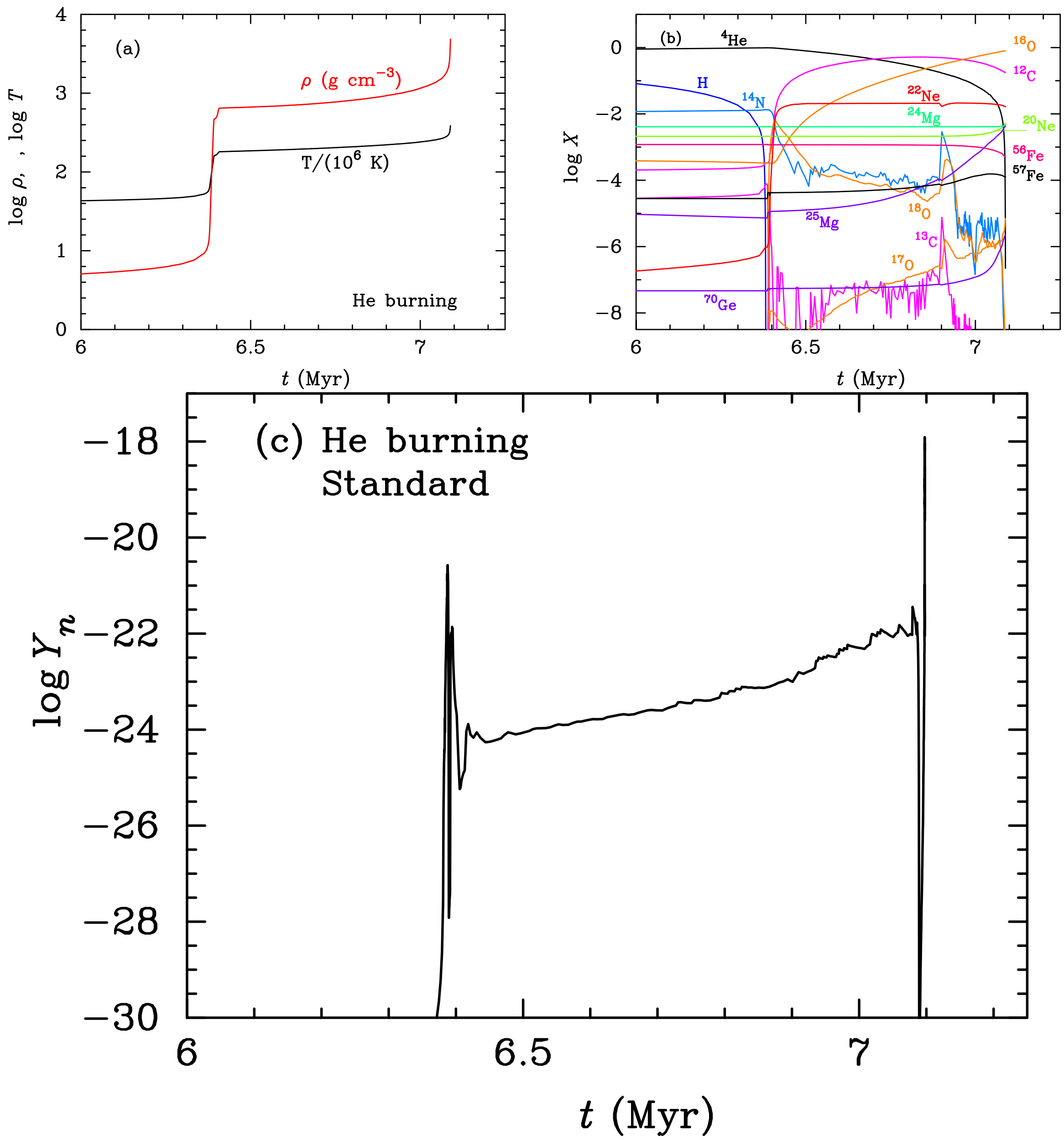

Figure 6. Results of physical quantities of a star with initial mass 25 $M_\odot$ and solar metallicity as a function of time during the core He burning at the stellar center with the "standard" rates of $^{16}O(n,\gamma)^{17}O$: (a) temperature and density in unit of 10^6 K and g cm^{-3} as indicated, (b) nuclear mass fractions, and (c) neutron mole fraction Y_n.

Table 3 shows production and destruction reactions of seven p-nuclei that have been overproduced at the end of He burning for the standard rate case. In addition, behaviors of abundance changes are commented. Most of p-nuclei evolve simply in either a production or a destruction dominated epoch, while the abundance of ^{115}Sn results through a complicated history. First its abundance is determined by a balance in the neutron capture series of $^{114}Sn(n,\gamma)^{115}Sn(n,\gamma)$. Then, the production dominated epoch follows by $^{115}In(\beta^-)$ and the destruction via (n,γ) becomes dominant in the end.

Figure 10 shows time evolution of mole fractions of the seven p-nuclei for the standard rate case. At $t \sim 6.4$ Myr, the H burning completes and the core temperature and density increase significantly (Figure 6(a)). A small amount of neutron release occurs then as a result of remnant ^{13}C burning via $^{13}C(\alpha, n)$. The subsequent neutron captures of s-nuclei temporarily populate isobars next to p-nuclei, and their decays lead to production of ^{108}Cd, ^{152}Gd, ^{158}Dy, and ^{164}Er. On the other hand, production of ^{113}In and ^{180}W occurs in the later time via the β-decay of ^{113}Cd and ^{180}Ta, respectively.

Figure 11 is the same as Figure 9 but at $M_r = 2M_\odot$ before the onset of the core Si burning. Through the C burning, abundances of nuclei with $A \lesssim 90$ increase significantly, while overproduction factors of nuclei with $A \gtrsim 90$ do not increase very much. In this high mass region, the abundance pattern has changed from that at the completion of the He burning. Overproduction factors of a part of s-only nuclei are reduced.

Figure 11(b) shows that some overproduction factors are smaller in the standard case than those in the KADoNiS case. In general, the larger the rates are at a given temperature, fewer neutrons are available for the s-process and abundances of the s-nuclei are less enhanced. However, these results reflect an accumulated effect of the time-dependent difference in the reaction rates of $^{16}O(n,\gamma)^{17}O$, and the resultant change in Y_n.

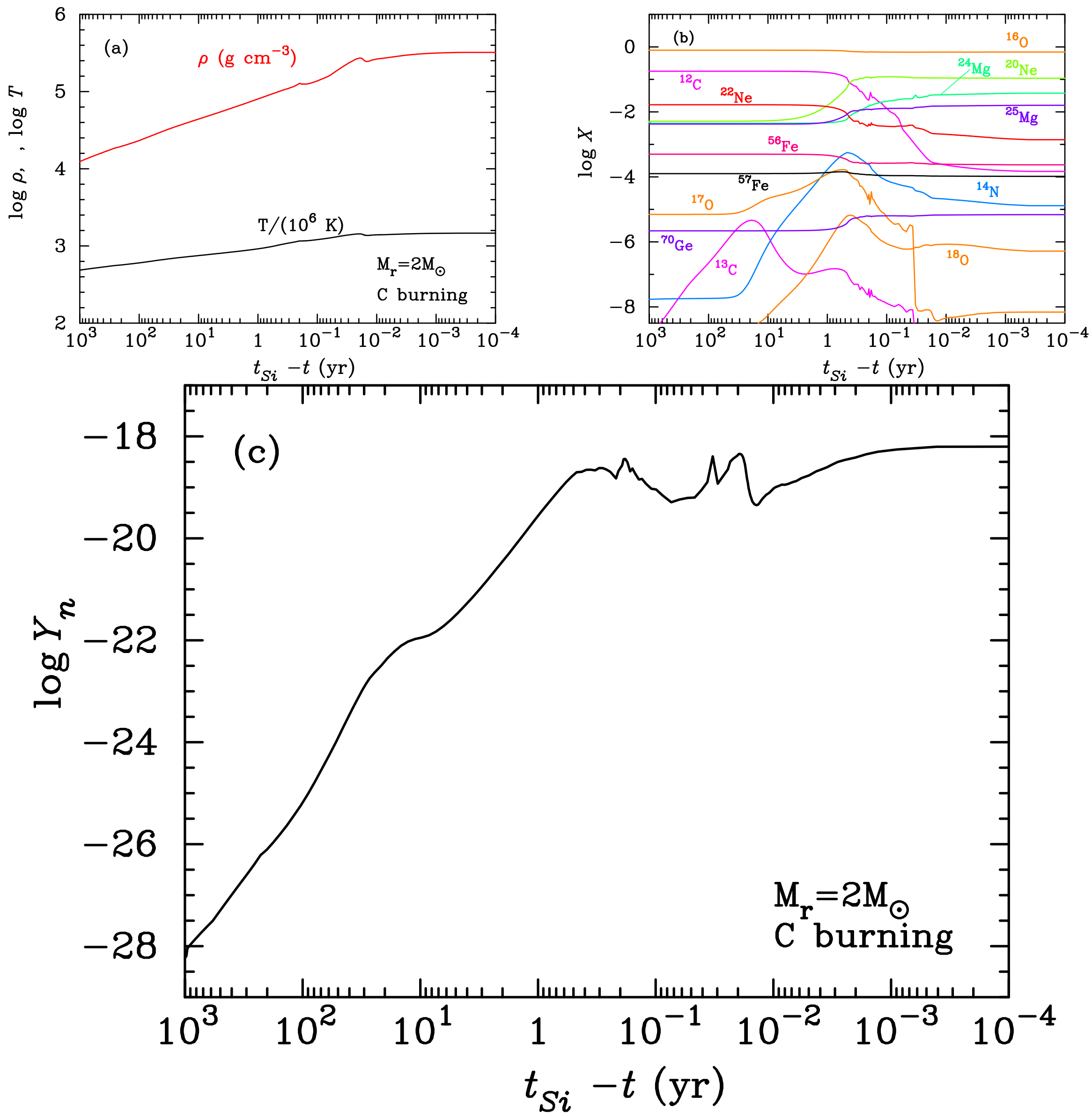

Figure 7. Same as Figure 6 but as a function of the time to the start of core Si burning, i.e., $t_{\mathrm{Si}} - t$ during the shell C burning at $M_r = 2M_\odot$.

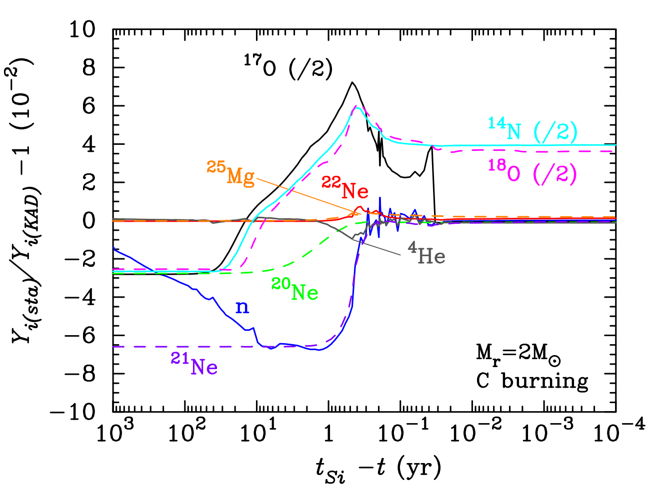

Figure 8. Deviations from unity of ratios of mole fractions of neutron, ^{4}He, ^{17,18}O, ^{20,21,22}Ne, and ^{25}Mg in the "standard" and KADoNiS cases as a function of the time to the start of core Si burning, i.e., $t_{\mathrm{Si}} - t$ during the shell C burning at $M_r = 2M_\odot$.

Only the ^{180}Ta is overproduced among *p*-nuclei. In the late time of $t_{\mathrm{Si}} - t \gtrsim 1$ yr, ^{180}Ta is produced via the ^{179}Ta(n,γ) reaction at $M_r = 2M_\odot$. The rarest nuclide in the solar system, ^{180}Ta is a very special *p*-nuclide; it has the 1^+ ground state with a short half-life $T_{1/2} = 8.154$ hr and the 9^- isomeric state with a half-life $T_{1/2} > 7.1 \times 10^{15}$ yr. The 1^+ ground state and the 9^- isomeric state are coupled through transitions to higher excited states, and their equilibrium populations are realized in thermal environment such as stellar interior at $k_{\mathrm{B}}T \approx 40$ keV (Mohr et al. 2007; Hayakawa et al. 2010). During the supernova (SN) explosion at the end of the massive star evolution, ^{180}Ta is easily destroyed via ^{180}Ta(γ, n). In fact, in the current calculation for the star with 25 $M_\odot$, the temperature is already high enough that photodisintegration reactions of ^{180}Ta(γ, n) and ^{181}Ta(γ, n) are the most strongly affecting the abundance evolution with comparable contributions from ^{179}Ta(n,γ) and ^{180}Ta(n,γ). Therefore, even if ^{180}Ta is produced in some significant amount by the completion of C burning, the final yield depends on the temperature and density evolution in later burning stages and the

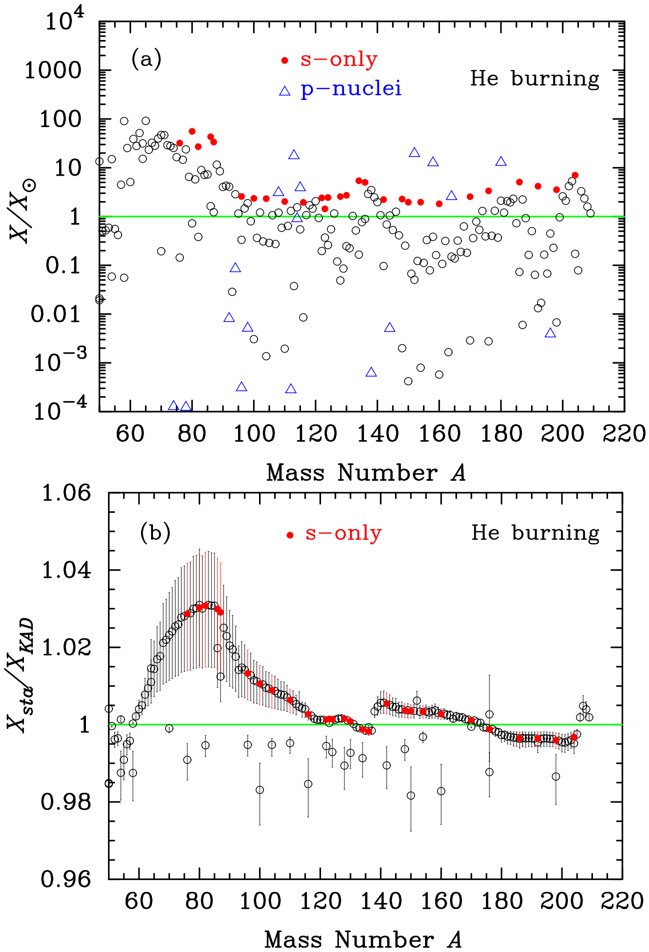

Figure 9. (a) Overproduction factors of stable nuclei as a function of mass number, at the stellar center after the core He burning in the standard rate case. Red filled circles and blue open triangles correspond to *s*-only nuclei and *p*-nuclei, respectively, while black open circles correspond to other stable nuclei. (b) Ratios of overproduction factors in the standard and KADoNiS cases: Red filled circles (*s*-only nuclei) and open circles (other stable nuclei). Ranges from the estimated uncertainty of the reaction rate are shown by vertical bars.

Table 3
Important Reactions of *p*-nuclei at the Start of He Burning

Nuclide	Production	Destruction	Behavior
^{108}Cd	^{108}Ag(β^-)	(n,γ)	production → destruction
^{113}In	^{113}Cd(β^-), ^{113}Sn(ε)	(n,γ)	destruction → production via ^{113}Cd(β^-)
^{115}Sn	^{114}Sn(n,γ), ^{115}In(β^-)	(n,γ)	balance of (n,γ) → production via ^{115}In(β^-) → destruction via (n,γ)
^{152}Gd	^{152}Eu(β^-)	(n,γ)	production → destruction
^{158}Dy	^{158}Tb(β^-)	(n,γ)	production → destruction
^{164}Er	^{164}Ho(β^-)	(n,γ)	production → destruction
^{180}W	^{180}Ta(β^-)	(n,γ)	destruction → production

explosion. It has been suggested that ^{180}Ta is produced in massive stars via photodisintegration, which operates in the late evolution stage (Arnould 1976) as well as during SNe (Woosley & Howard 1978). However, the final yield is often estimated to be significantly smaller than the level required to explain the solar abundance of ^{180}Ta (Woosley & Howard 1978; Rayet et al. 1990, 1995). The neutrino process in SNe II (Woosley et al. 1990; Heger et al. 2005) and the Galactic cosmic ray

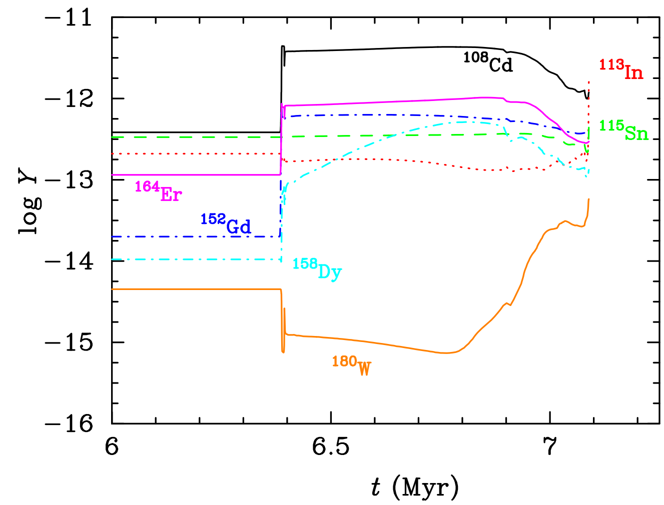

Figure 10. Mole fractions of *p*-nuclei as a function of time during the core He burning at the stellar center for the same model as in Figure 6.

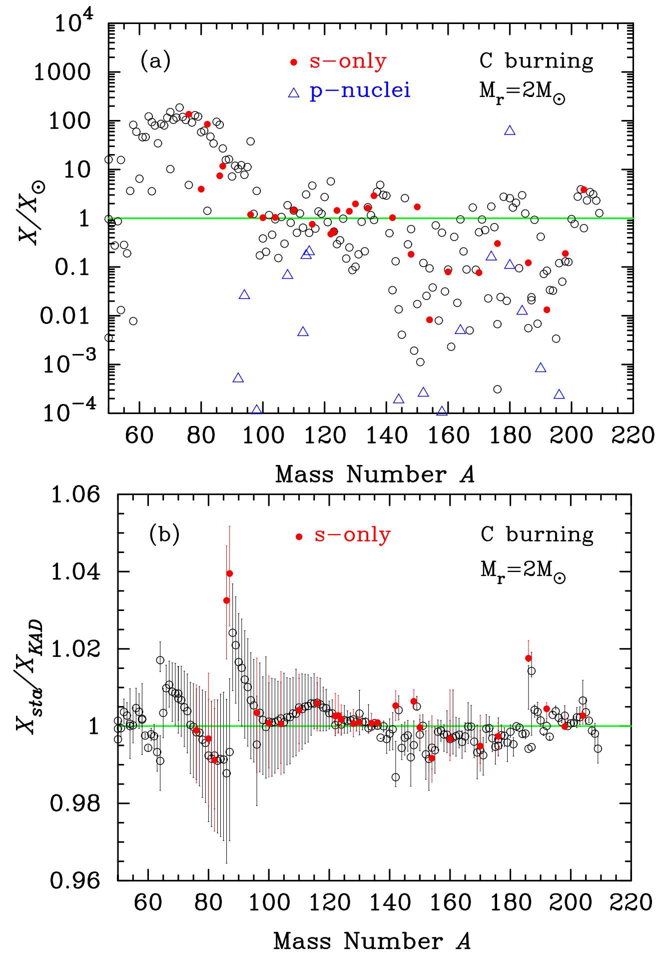

Figure 11. Same as Figure 9 but at $M_r = 2M_\odot$ before the onset of the core Si burning.

nucleosynthesis (Audouze 1970) contribute significantly to the solar system content of ^{180}Ta. According to a recent calculation, the spallation ^{181}Ta(p, pn)^{180}Ta and the charge exchange ^{180}Hf(p, n)^{180}Ta by Galactic cosmic rays explain about 20% of solar abundance of ^{180}Ta (Kusakabe & Mathews 2018).

4. Conclusion

We reinvestigate the neutron capture reaction of ^{16}O from viewpoints of nuclear structure and the stellar nucleosynthesis. The contributions from s.p. resonances to total capture CSs are quantitatively considered in Breit–Wigner formalism, together with the interference term between DC and resonant CSs being taken into account. It turns out that the interference term is crucial for the description of the behavior below and above the resonance energies, and DC dominates the reaction rates in the lower-energy region. The differences of the reaction rates between our predictions and other available results are prominent, about 10%–25% for the higher-energy region in comparison with the KADoNiS database and the latest data evaluations.

The sensitivity of the weak *s*-process to the reaction rates of ^{16}O(n,γ) was studied in a multi-zone post-process nucleosynthesis calculation for the core He- and shell C-burning stages of a 25 $M_\odot$ star. A change in the rate of ^{16}O(n,γ)^{17}O for $T_9 \gtrsim 0.5$ within the estimated uncertainty leads to smaller abundances of neutron and ^{17}O. However, it is observed that at the position of $M_r = 2M_\odot$, the neutron abundance becomes slightly larger immediately before the core Si burning as a result of survival of more ^{22}Ne nuclei. We obtain the resultant change up to 4% in abundances of *s*-nuclei between two cases of the reaction rates. At the low temperature of the He-burning stage, the new rate derived in this study leads to abundances of *s*-nuclei larger than those for the larger KADoNiS v0.3 rate. At the high temperature of the C-burning stage, the reaction rate is significantly higher in the standard case, and abundance excesses of *s*-nuclei are significantly modified. We note that the current revision of the ^{16}O(n,γ) rate results in species-dependent changes of *s*-nuclear abundances (Figure 11(b)), reflecting a change of relative importance of the neutron captures in the He and C burnings.

Discussions with Prof. Tatsushi Shima, Prof. Satoshi Chiba, and Prof. Kouichi Hagino are gratefully acknowledged. We are grateful that the editor Dr. Daniel Wolf Savin contacted Dr. Peter Mohr, who kindly shared experimental data. This work was partially supported by the National Natural Science Foundation of China (NSFC) under grants No. 11375022, No. 11175216, No. 11575060, No. 11435014, and No. 11235002. This work is also supported by the NSFC Research Fund for International Young Scientists (grant No. 11850410441) and in part by Grants-in-Aid for Scientific Research of the Japan Society for the Promotion of Science (JSPS) No. 15H03665, No. 17K05459, and No. 20K03958.

Software: MESA (version r11701 Paxton et al. 2011).

Appendix A
Reactions of C to Mg Relevant to the *s*-process in the C Burning

We show detailed information on nucleosynthesis of light nuclei from C to Mg in the C burning in the adopted stellar model. It is found that the uncertainty in the rate of ^{16}O(n,γ)^{17}O affects the *s*-process as follows. A larger reaction rate leads to a larger ^{17}O abundance and smaller n abundance. The *s*-process is less efficient in the early epoch. The enhanced ^{17}O abundance results in a smaller α abundance because of the capture via ^{17}O(α, n)^{20}Ne. During the C burning ∼1–0.1 yr before the onset of Si burning, more ^{22}Ne nuclei survive from weaker destruction via ^{22}Ne(α, n). It induces a larger neutron abundance and more efficient *s*-process in the late epoch of C burning.

Table A1 shows the important destruction and production reactions during the C burning at $\Delta t_{\rm Si} \equiv t_{\rm Si} - t \sim$ 1–0.1 yr for respective isotopes of C to Mg. This analysis clarifies how the uncertainty in the reaction rate of ^{16}O(n,γ)^{17}O affects the *s*-process nucleosynthesis in the adopted model for a star with $M = 25M_\odot$.

Figure A1 shows the amplitudes of abundance change rates for ^{16}O (panel (a)), ^{17}O (b), and ^{22}Ne (c) as a function of $\Delta t_{\rm Si}$.

A.1. Late Phase of He Burning $\Delta t_{Si} > 10^4$ yr

At low temperatures during the He burning, the standard rate of the reaction ^{16}O(n,γ)^{17}O is smaller than the KADoNiS rate. Then, ^{17}O abundance becomes smaller. The ^{21}Ne abundance increases at $\Delta t_{\rm Si} \sim 3 \times 10^5$ yr via ^{17}O(α,γ) resulting in a deficiency in the ^{21}Ne abundance compared to the KADoNiS rate case. Since ^{20}Ne is partially produced via ^{17}O(α, n), its deficiency also grows at $\Delta t_{\rm Si} \gtrsim 3 \times 10^4$ yr. In addition, deficiencies of ^{14}N and ^{18}O emerge at $\Delta t_{\rm Si} \gtrsim 1 \times 10^4$ yr from the nuclear flows ^{17}O(p,α)^{14}N and ^{17}O(n,γ)^{18}O, respectively. Reflecting the smaller rate of ^{16}O(n,γ)^{17}O, Y_n is larger in the standard rate case until $\Delta t_{\rm Si} \sim 4 \times 10^3$ yr. However, along with increasing temperature, the standard rate becomes larger than the KADoNiS rate and Y_n becomes larger. As a result of such an evolution of light nuclear abundances, there are differences in abundances before the C burning as shown in the earlier phase in Figure 8.

A.2. Early Phase of $\Delta t_{Si} \gtrsim 1$ yr

When the C burning starts, the reaction ^{16}O(n,γ)^{17}O is the second largest destruction reaction of ^{16}O and the largest production reaction of ^{17}O. Therefore, the ^{16}O abundance slightly decreases, the ^{17}O abundance significantly increases, and the neutron abundance decreases. In the early epoch of $\Delta t_{\rm Si} \gg 1$ yr, the yield of ^{17}O is smaller than the initial abundance. In addition, the neutron absorption by ^{16}O is relatively weak at low temperatures. Therefore, the fractional deficiency of ^{17}O abundance stays constant and the deficiency of neutron abundance in Figure 8 are smaller at $\Delta t_{\rm Si} \gg 1$ yr.

At $\Delta t_{\rm Si} \sim 10$ yr, the increase of ^{17}O abundance via ^{16}O(n,γ) becomes significant (Figure A1(b)). The fractional increase (or excess) of the ^{17}O abundance starts increasing (Figure 8). Excesses of ^{14}N and ^{18}O abundances also occur coherently from that of ^{17}O. This is because ^{14}N is produced via ^{17}O(p,α), and ^{18}O is produced primarily via ^{14}N(α,γ)^{18}F(,β^+) and secondarily via ^{14}C(α,γ).

The excess in the ^{17}O abundance thus results in an excess in abundances of ^{14}N, ^{18}O, and ^{18}F (Figure 8).

At $\Delta t_{\rm Si} \gtrsim 0.3$ yr, the destruction of ^{17}O is dominated by the reactions ^{17}O(α, n)^{20}Ne and ^{17}O(p,α)^{14}N. As the Si burning approaches, a more fraction of ^{17}O nuclei produced via ^{16}O(n,γ) are destroyed via ^{17}O(γ, n) (Figure A1(b)). At $\Delta t_{\rm Si} \lesssim 1$ yr, the reaction ^{17}O(α, n) is a source of neutrons with its rate smaller than that of ^{22}Ne(α, n) by a factor of $\gtrsim$2. When the ^{17}O abundance is increased (Figure 8), the neutron production rate via ^{17}O(α, n) is increased, and Y_α is decreased by a larger capture rate. The rate of ^{17}O(α, n) then decreases as a result of the negative feedback.

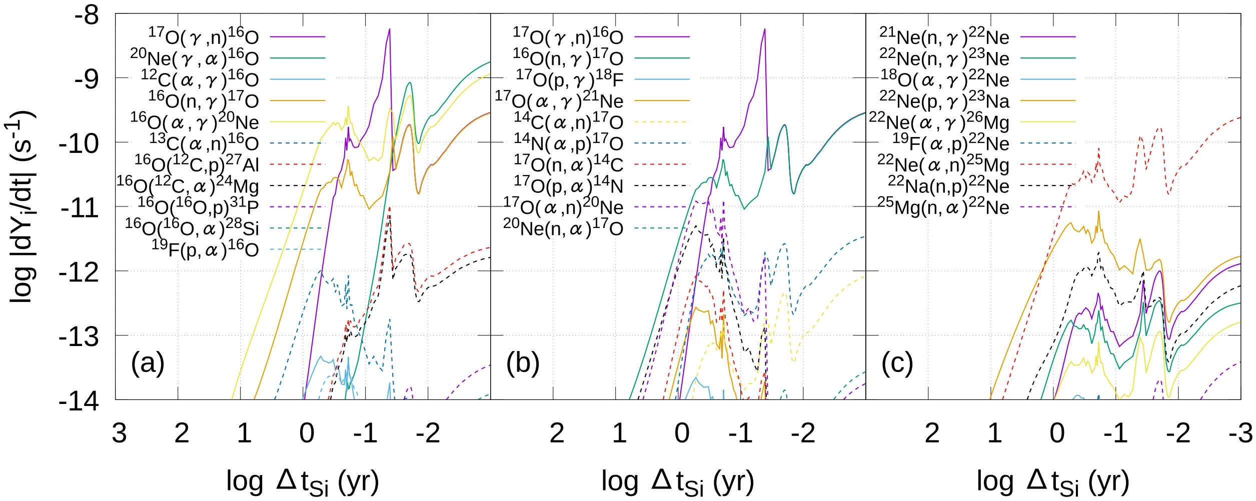

Figure A1. Amplitudes of abundance change rates, i.e., $|dY_i/dt|$ as a function of time to the onset of Si burning for $i = {}^{16}$O (a); ^{17}O (b); and ^{22}Ne (c).

Table A1
Important Reactions of C to Mg at $t_{Si} - t \sim 1$–0.1 s

Nuclide	Destruction	Production
^{12}C	^{12}C(^{12}C,p)^{23}Na, ^{12}C(^{12}C,α)^{20}Ne, ^{12}C(p,γ)^{13}N	^{13}N(γ, p)
^{13}C	^{13}C(α, n)^{16}O	…
^{14}C	^{14}C(α,γ)^{18}O	^{14}N(n, p), ^{17}O(n, α)
^{14}N	^{14}N(α,γ)^{18}F, ^{14}N(α, p)^{17}O, ^{14}N(n, p)^{14}C	^{17}O(p,α)
^{15}N	^{15}N(p,α)^{12}C	^{18}O(p,α)
^{16}O	^{16}O(α,γ)^{20}Ne, ^{16}O(n,γ)^{17}O	^{17}O(γ, n)[a]
^{17}O	^{17}O(α, n)^{20}Ne, ^{17}O(p,α)^{14}N, ^{17}O(n, α)^{14}C, ^{17}O(γ, n)^{16}O[a]	^{16}O(n,γ)
^{18}O	^{18}O(n,γ)^{19}O, ^{18}O(α, n)^{21}Ne	^{18}F(,β^+), ^{14}C(α,γ)
^{19}F	^{19}F(α, p)^{22}Ne	^{22}Na(n, α), ^{15}N(α,γ)
^{20}Ne	…	^{16}O(α,γ), ^{12}C(^{12}C,α),^{23}Na(p,α)
^{21}Ne	^{21}Ne(α, n)^{24}Mg, ^{21}Ne(p,γ)^{22}Na	^{20}Ne(n,γ)
^{22}Ne	^{22}Ne(α, n)^{25}Mg, ^{22}Ne(p,γ)^{23}Na	^{22}Na(n, p)[b]
^{22}Na	^{22}Na(n, p)^{22}Ne	^{21}Ne(p,γ)
^{23}Na	^{23}Na(p,α)^{20}Ne	^{12}C(^{12}C,p)
^{24}Mg	^{24}Mg(n,γ)^{25}Mg	^{20}Ne(α,γ), ^{21}Ne(α, n), ^{23}Na(p,γ), ^{24}Na(,β^-)
^{25}Mg	^{25}Mg(n,γ)^{26}Mg, ^{25}Mg(p,γ)^{26}Al	^{22}Ne(α, n), ^{24}Mg(n,γ)
^{26}Mg	^{26}Mg(p,γ)^{27}Al	^{25}Mg(n,γ), ^{26}Al(,β^+), ^{23}Na(α, p)

Notes.
[a] Important only in the late time.
[b] Much smaller than the destruction rate.

A.3. Late Phase of $\Delta t_{Si} \lesssim 1$ yr

The abundance of the α particle, Y_α, is affected. The α-capture rate is dominated by the reaction ^{16}O(α,γ)^{20}Ne, but also significantly contributed to by ^{22}Ne(α, n)^{25}Mg and ^{17}O(α, n)^{20}Ne. Therefore, the larger ^{17}O abundance leads to a slightly larger destruction rate of α particle at $\Delta t_{Si} \sim 1$–0.2 yr.

Excesses of ^{22}Ne and ^{25}Mg abundances are induced at $\Delta t_{Si} \lesssim 1$ yr. ^{22}Ne is produced weakly via ^{22}Na(n, p)^{22}Ne with decreased Y_n, and destroyed strongly via ^{22}Ne(α, n)^{25}Mg and subdominantly via ^{22}Ne(p,γ)^{23}Na. Because the abundance Y_α is small, the ^{22}Ne abundance becomes small. ^{25}Mg is strongly produced via ^{22}Ne(α, n) and subdominantly via ^{24}Mg(n,γ), and destroyed weakly via ^{25}Mg(n,γ)^{26}Mg and subdominantly via ^{25}Mg(p,γ)^{26}Al. Therefore, the larger ^{22}Ne abundance leads to a larger ^{25}Mg abundance.

The increase of ^{20}Ne abundance (Figure 7(b)) originates predominantly from the reactions ^{16}O(α,γ), ^{12}C(^{12}C,α), and ^{23}Na(p,α). Abundances of ^{12}C and ^{16}O are almost insensitive to the reaction rate of ^{16}O(n,γ)^{17}O. The p, α, and ^{23}Na are products from the ^{12}C+^{12}C fusion, and their yields are limited by the ^{12}C abundance. As a result, the total yield of ^{20}Ne in the C burning is not changed through these reactions. However, an increased production via ^{17}O(α, n) leads to a reduction of the ^{20}Ne deficiency. A significant fraction of the production for ^{20}Ne comes from the reaction ^{17}O(α, n)^{20}Ne. Through the sequence of ^{16}O(n,γ)^{17}O(α, n)^{20}Ne, most of the captured neutrons are released, and resulting in an enhancement of ^{20}Ne production rate.

At $\Delta t_{Si} \lesssim 0.3$ yr, the ^{17}O excess caused by the increased rate for ^{16}O(n,γ)^{17}O suddenly decreases (Figure 8). In this epoch, the temperature temporarily increases (Figure 7(a)), and the destruction via ^{17}O(γ, n) dominates over the production via ^{16}O(n,γ) (Figure A1(b)). At $\Delta t_{Si} \sim 0.03$ yr, the production and destruction balance each other. Because neutrons are significantly released from ^{17}O at the high temperature, Y_n ends up in some excess at $\Delta t_{\rm Si} \gtrsim 1$ yr (Figure 8). Thus, ^{17}O can be regarded as a reservoir of neutrons. It is to be noted that the neutron production rate via ^{17}O(γ, n) is much higher than that via ^{22}Ne(α, n) at $\Delta t_{\rm Si} = 0.3$–0.03 yr. According to this decrease of the ^{17}O excess, excesses in ^{14}N and ^{18}O abundances reduce as well. The recovery of Y_n leads to an enhanced production rate of ^{21}Ne via ^{20}Ne(n,γ). As a result, the ^{21}Ne abundance is increased at $\Delta t_{\rm Si} \lesssim 0.3$ yr.

At $\Delta t_{\rm Si} \lesssim 0.4$ yr, the ^{22}Ne excess decreases temporarily. In this epoch, there is still a deficiency of Y_n. It reduces the production rate via ^{22}Na(n, p), which is a subdominant production reaction of ^{22}Ne during the ^{22}Ne burning operating at that time (Figure 7(b)). Because of the reduction, the ^{22}Ne excess slightly decreases. The deficiency in Y_α grows at $\Delta t_{\rm Si} \lesssim 1$ yr, and returns to almost zero at $\Delta t_{\rm Si} \sim 0.3$ yr. Then, the difference in the ^{22}Ne destruction rate via ^{22}Ne(α, n) becomes small. Therefore, although the ^{22}Ne destruction is still operative in this epoch (Figure 7(b)), the excess of the ^{22}Ne abundance stays constant after the Y_α becomes the same.

ORCID iDs

Shi-Sheng Zhang https://orcid.org/0000-0003-3926-7151
Motohiko Kusakabe https://orcid.org/0000-0003-3083-6565
Toshitaka Kajino https://orcid.org/0000-0002-8619-359X

References

Aoki, W., Ryan, S. G., Norris, J. E., et al. 2001, APJ, 561, 346
Arnould, M. 1976, A&A, 46, 117
Audouze, J. 1970, A&A, 8, 436
Bao, Z. Y., Beer, H., Käppeler, F., et al. 2000, ADNDT, 76, 70
Bennett, M. E., Hirschi, R., Pignatari, M., et al. 2010, JPhCS, 202, 012023
Best, A., Beard, M., Görres, J., et al. 2013, PhRvC, 87, 045805
Bisterzo, S., Gallino, R., Käppeler, F., et al. 2015, MNRAS, 449, 506
Bisterzo, S., Travaglio, C., Gallino, R., Wiescher, M., & Käppeler, F. 2014, APJ, 787, 10
Buchler, J. R., & Yueh, W. R. 1976, ApJ, 210, 440
Burbidge, M. E., Burbidge, G. R., Fowler, W. A., & Hoyle, F. 1957, RvMP, 29, 547
Cameron, A. G. W. 1957, Lecture in Purdue University
Cassisi, S., Potekhin, A. Y., Pietrinferni, A., Catelan, M., & Salaris, M. 2007, ApJ, 661, 1094
Chugunov, A. I., DeWitt, H. E., & Yakovlev, D. G. 2007, PhRvD, 76, 025028
Clayton, D. D. 1984, Principles of Stellar Evolution and Nucleosynthesis for the Year 1984 (Chicago, IL: Univ. Chicago Press)
Cyburt, R. H., Amthor, A. M., Ferguson, R., et al. 2010, ApJS, 189, 240
Dillmann, I., Heil, M., Käppeler, F., et al. 2006, in AIP Conf. Proc. 819, KADoNiS- The Karlsruhe Astrophysical Database of Nucleosynthesis in Stars, ed. A. Woehr & A. Aprahamian (Melville, NY: AIP), 123
Dillmann, I., Plag, R., Käppeler, F., & Rauscher, T. 2009, in Proc. EFNUDAT (European Facilities for Nuclear Data Measurements) Scientific Workshop on Neutron Measurements, Theory and Applications, ed. F.-J. Hambsch (Luxembourg: Publications Office of the European Union (2009)), 55
Ferguson, J. W., Alexander, D. R., Allard, F., et al. 2005, ApJ, 623, 585
Firestone, R. B., & Revay, Zs. 2016, PhRvC, 93, 044311
Frischknecht, U., Hirschi, R., Rauscher, T., et al. 2010, in Nuclei in the Cosmos 11 (Trieste: SISSA), 189
Fuller, G. M., Fowler, W. A., & Newman, M. J. 1985, ApJ, 293, 1
Gallino, R., Arlandini, C., Busso, M., et al. 1998, APJ, 497, 388
Hayakawa, T., Kajino, T., Chiba, S., et al. 2010, PhRvC, 81, 052801
Heger, A., Kolbe, E., Haxton, W. C., et al. 2005, PhLB, 606, 258
Heil, M., Juseviciute, A., Käppeler, F., et al. 2009, PASA, 26, 243
Heil, M., Käppeler, F., Uberseder, E., et al. 2008, PhRvC, 77, 015808
Hirschi, R. 2007, A&A, 461, 571
Holt, R., Jackson, H., Laszewski, R., Monahan, J., & Specht, J. 1978, PhRvC, 18, 1962
Huang, J. T., Bertulani, C. A., & Guimaraes, V. 2010, ADNDT, 96, 824
Iben, I., & Renzini, A. 1982, ApJL, 263, L23
Iben, I., Jr. 1975, APJ, 196, 525
Igashira, M., Nagai, Y., Masuda, K., & Ohsaki, T. 1995, ApJL, 441, L89
Iglesias, C. A., & Rogers, F. J. 1993, ApJ, 412, 752
Iglesias, C. A., & Rogers, F. J. 1996, ApJ, 464, 94
Itoh, N., Hayashi, H., Nishikawa, A., & Kohyama, Y. 1996, ApJS, 102, 411
Jeukenne, J. P., Lejeune, A., & Mahaux, C. 1977, PhRvC, 16, 80
Johnson, R. G., Berman, B. L., McNeill, K. G., et al. 1979, PhRvC, 20, 27
Käppeler, F., Gallino, R., Bisterzo, S., & Aoki, W. 2011, RvMP, 83, 157
Karakas, A. I., & Lugaro, M. 2016, APJ, 825, 26
Koloczek, A., Thomas, B., Glorius, J., et al. 2016, ADNDT, 108, 1
Koning, A. J., & Delaroche, J. P. 2003, NuPhA, 713, 231
Kusakabe, M., & Mathews, G. J. 2018, ApJ, 854, 183
Lamb, S. A., Howard, W. M., Truran, J. W., et al. 1977, ApJ, 217, 213
Langanke, K., & Martinez-Pinedo, G. 2000, NuPhA, 673, 481
Lodders, K., Palme, H., & Gail, H.-P. 2009, LanB, 4, 712
Mathews, G. J., Mengoni, A., Thielemann, F. K., & Fowler, W. A. 1983, APJ, 270, 740
Meynet, G., Ekström, S., & Maeder, A. 2006, A&A, 447, 623
Meynet, G., & Maeder, A. 2002, A&A, 390, 561
Mohr, P., Heinz, C., Pignatari, M., et al. 2016, APJ, 827, 29
Mohr, P., Käppeler, F., & Gallino, R. 2007, PhRvC, 75, 012802
Nagai, Y., Igashira, M., Shima, T., et al. 1995, in AIP Conf. Proc. 327, Proc. Nuclei in the Cosmos 1994, ed. M. Busso, R. Gallino, & C. Raiteri (Melville, NY: AIP), 201
Nagai, Y., Igashira, M., Shima, T., et al. 2020, to be published
Nishimura, N., Hirschi, R., Rauscher, T., et al. 2017, MNRAS, 469, 1752
Oda, T., Hino, M., Muto, K., Takahara, M., & Sato, K. 1994, ADNDT, 56, 231
Ozawa, A., Suzuki, T, & Tanihata, I. 2001, NuPhA, 693, 32
Paxton, B., Bildsten, L., Dotter, A., et al. 2011, ApJS, 192, 3
Paxton, B., Marchant, P., Schwab, J., et al. 2015, ApJS, 220, 15
Paxton, B., Schwab, J., Bauer, E. B., et al. 2018, ApJS, 234, 34
Paxton, B., Smolec, R., Schwab, J., et al. 2019, ApJS, 243, 10
Peters, J. G., Fowler, W. A., & Clayton, D. D. 1972, ApJ, 173, 637
Pignatari, M., Gallino, R., Heil, M., et al. 2010, APJ, 710, 1557
Pignatari, M., Gallino, R., Meynet, G., et al. 2008, ApJL, 687, L95
Pols, O. R., Tout, C. A., Eggleton, P. P., & Han, Z. W. 1995, MNRAS, 274, 964
Potekhin, A. Y., & Chabrier, G. 2010, CoPP, 50, 82
Prantzos, N., Hashimoto, M., & Nomoto, K. 1990, A&A, 234, 211
Raiteri, C. M., Busso, M., Gallino, R., et al. 1991, ApJ, 371, 665
Raiteri, C. M., Gallino, R., Busso, M., et al. 1993, ApJ, 419, 207
Rayet, M., Arnould, M., Hashimoto, M., Prantzos, N., & Nomoto., K. 1995, A&A, 298, 517
Rayet, M., Prantzos, N., & Arnould, M. 1990, A&A, 227, 271
Reifarth, R., Lederer, C., & Käpeler, F. 2014, JPhG, 41, 053101
Rogers, F. J., & Nayfonov, A. 2002, ApJ, 576, 1064
Saumon, D., Chabrier, G., & van Horn, H. M. 1995, ApJS, 99, 713
Sharma, M. M., Nagarajan, M. A., & Ring, P. 1993, PhLB, 312, 377
Sun, T. T., Zhang, S. Q., Zhang, Y., Hu, J. N., & Meng, J. 2014, PhRvC, 90, 054321
Takahashi, K., & Yokoi, K. 1987, ADNDT, 36, 375
The, L.-S., El Eid, M. F., & Meyer, B. S. 2007, ApJ, 655, 1058
Timmes, F. X., & Swesty, F. D. 2000, ApJS, 126, 501
Townsend, R. 2019, MESA SDK for Linux, Zenodo, doi:10.5281/zenodo.2669541
Trkov, A., & Brown, D. A. 2018, ENDF-102 : ENDF/B Formats Manual, Tech. Rep. BNL-203218-2018-INRE, National Nuclear Data Center (CCXV Edition, ENDF/B-VI, ENDF/B-VII and ENDF/B-VIII Library)
Truran, J. W., & Iben, I., Jr. 1977, APJ, 216, 797
Woosley, S. E., Hartmann, D. H., Hoffman, R. D., & Haxton, W. C. 1990, ApJ, 356, 272
Woosley, S. E., & Howard, W. M. 1978, ApJS, 36, 285
Xu, R. R., Ma, Z. Y., Zhang, Y., et al. 2016, PhRvC, 94, 034606
Xu, Y., & Goriely, S. 2012, PhRvC, 86, 045801
Yamamoto, K., Masui, H., Kato, K., et al. 2009, PThPh, 121, 375
Zhang, S. S., Peng, J. P., Smith, M. S., Arbanas, G., & Kozub, R. L. 2015, PhRvC, 91, 045802